Mechanics Research Communications 143 (2025) 104351

Contents lists available at ScienceDirect

Mechanics Research Communications

journal homepage: www.elsevier.com/locate/mechrescom

Piezoelectric flutter energy harvesting: Absolute nodal coordinate formulation model and wind tunnel experiment

Taisei Mukogawa [a,*], Kento Shimura [a], Shuonan Dong [a], Koji Fujita [b], Hiroki Nagai [c], Masaki Kameyama [d], Yu Shi [e], Yu Jia [f], Constantinos Soutis [g], Hiroki Kurita [h], Fumio Narita [h], Yushin Hara [a], Kanjuro Makihara [a], Keisuke Otsuka [a,*]

[a] Department of Aerospace Engineering, Tohoku University, 6-6-01, Aramaki-Aza-Aoba, Aoba-Ward, Sendai, Japan
[b] Kanazawa Institute of Technology, 7-1, Ohgigaoka, Nonoichi, Japan
[c] Institute of Fluid Science, Tohoku University, 2-1-1, Katahira Aoba-Ward, Sendai, Japan
[d] Department of Mechanical Systems Engineering, Shinshu University, 4-17-1, Wakasato, Nagano, Japan
[e] Leeds Institute of Textiles and Colour (LITAC), School of Design, University of Leeds, Woodhouse Lane, Leeds LS2 9JT, United Kingdom
[f] College of Engineering and Physical Sciences, Aston University, Birmingham, United Kingdom
[g] Aerospace Research Institute, University of Manchester, Manchester, United Kingdom
[h] Department of Frontier Sciences for Advanced Environment, Tohoku University, Sendai, Japan

ARTICLE INFO

Keywords:
Absolute nodal coordinate formulation
Wind tunnel experiment
Flutter
Energy harvesting
Unsteady vortex lattice method

ABSTRACT

This study proposes a new flutter harvesting analysis framework based on an absolute nodal coordinate formulation (ANCF) model that includes a nonlinear finite element method, a three-dimensional unsteady vortex lattice method that considers nonlinearities, and a piezoelectric equation. Because conventional studies assumed no extensionality of the neutral axis, use of flutter harvester configurations was restricted. However, this framework using the ANCF model can be applied to different configurations (e.g., extensible harvesters with fixed-fixed boundaries or multibody harvesters). The feasibility of the proposed method was verified by conducting wind tunnel experiments. The frequencies, root mean square (RMS) displacements, and RMS voltages of the analysis and experiment were compared. The difference between experiment and analysis was 23% in terms of frequencies. One of the reasons for the difference was viscous drag. Although the results were not a perfect match, the introduction of a viscous drag model will be considered in future studies to enhance this framework.

1. Introduction

With the recent shift to the Internet of Things (IoT) and the focus on compact power generation devices, abundant research has been conducted on energy harvesting [1]. Environmental energy exists in various forms, including light, heat, electromagnetic fields, and mechanical vibration. Several mechanisms, such as piezoelectric, electromagnetic, electrostatic, frictional electric, and magnetostrictive, have been used to power generation using mechanical vibration. In addition, different forms of power generation using vibrations excited by fluids are available [2–4]. Flutter energy harvesting, which is the subject of this study, uses self-excited vibrations caused by aeroelastic instability.

The recent trend of IoT requires diverse wireless energy sources. Therefore, the relatively high amplitude of flutter limit cycle oscillation (LCO) may become one of the new energy sources. As a result, studies on harvesting flutter energy have witnessed a recent increase.

Dunnmon et al. [5] studied flutter harvesting using flexible bodies, wherein they stated that cantilevered beam harvesters in axial flow possess a simple structure and can be easily fabricated. In addition, they performed an analysis using a linear unsteady vortex lattice method (UVLM) and stated that their theoretical predictions agreed with the experimental results. The medium-fidelity UVLM [6], which is based on the potential flow assumption, can calculate unsteady aerodynamic forces. The calculation by the UVLM method is faster than that by higher-fidelity computational fluid dynamics methods. Therefore, the UVLM has been widely used for aeroelastic analysis. Dunnmon et al. [5] demonstrated that using the LCO of the flutter may help harvest energy while avoiding structural damage. Tang et al. [7] performed a flutter energy-harvesting analysis in accordance with the mass and stiffness of a piezoelectric patch and showed a correlation between the experiment

* Corresponding authors.
E-mail addresses: taisei.mukogawa.q3@dc.tohoku.ac.jp (T. Mukogawa), keisuke.otsuka.d6@tohoku.ac.jp (K. Otsuka).

https://doi.org/10.1016/j.mechrescom.2024.104351
Received 14 March 2024; Received in revised form 23 September 2024; Accepted 29 November 2024
Available online 30 November 2024

and analysis. These studies [5,7] were formulated under the similar assumption that the neutral axis is not extensible.

In this study, we focused on a flutter energy-harvesting analysis involving an absolute nodal coordinate formulation (ANCF) model [8,9] without assuming no extensibility of the neutral axis. ANCF is a nonlinear finite element method that is characterized by a constant mass matrix, which allows an efficient dynamic analysis. Because the constraint equations for various mechanical joints can be written in simple linear or quadratic nonlinear forms, the ANCF model may be easily applied to multibody systems. Moreover, the aerodynamic/contact loading points may be derived through a simple multiplication of a shape function and a generalized nodal coordinate vector. Due to these advantages, the ANCF model has been widely adopted in various engineering applications over the past two decades [10]. For example, Bulín et al. [11] simulated a system of driven weights connected to pulleys through flexible cables modeled using ANCF; the experimental outcomes agreed well with the simulated outcomes. Tao et al. [12] used an ANCF to simulate the dynamic response of origami with complex deformations.

Several studies have been conducted on the coupling of ANCF and piezoelectricity. Nada and El-Assal [13] performed static and dynamic analyses of a beam-attached piezoelectric actuator and sensor. The outcomes of the ANCF analysis showed good agreement with the solution obtained from the COMSOL software. Guo et al. [14] simulated the large deformation behavior of a folded structure using ANCF. They demonstrated that applying different voltages to a piezoelectric actuator can transform a flexible beam according to the desired shape. However, Nada and El-Assal [13] and Guo et al. [14] did not describe the formulation of the voltage and electric charge of the entire piezoelectric patch when it was divided into elements.

Considerable research has been conducted on the coupling of ANCF and UVLM. Otsuka et al. [15] analyzed the deployment motion of multibody wings using ANCF and UVLM, and they validated the analysis by conducting wind tunnel experiments. In addition, they studied aeroelastic oscillation (not LCO) using ANCF and UVLM and validated the accuracy of this method by conducting wind tunnel experiments [16]. Yamano et al. [17] analyzed the LCO of a flutter windmill using ANCF and UVLM. In their study, they assumed that the energy lost due to material damping was equivalent to the electric energy gained from the flutter windmill. The analysis results were compared with the reference experimental data. Because they used reference experimental data rather than conducting their experiment, some parameters (e.g., material damping property) were unavailable. Thus, discussing the difference between the analysis and experimental results was difficult.

Table 1 shows a comparison between previous and present studies. The coupling of ANCF with UVLM and ANCF with piezoelectricity was conducted. However, no flutter-harvesting analysis framework based on ANCF coupled with UVLM and piezoelectricity is available. Moreover, this flutter-harvesting framework has not been experimentally validated.

The two main objectives of the study are as follows. The first objective is to develop a new flutter-harvesting analysis framework based on ANCF, UVLM, and piezoelectricity for the harvester, as shown in Fig. 1 (a). The harvester possesses a piezoelectric patch attached to the beam. The beam is fixed to a jig in a direction parallel to the flow, with the coordinate axes *XYZ* defined as shown in Fig. 1 (a). Fig. 1 (b) shows a model of the harvester, including the circuit. The airflow is horizontal to the harvester. The harvester oscillates in the *Z*-direction. The electrodes of the piezoelectric patch are aligned vertically along the flow direction. Most previous studies on flutter harvesting have adopted Euler-Bernoulli beams as the structural model, assuming no extensionality of the neutral axis. The ANCF used in this study can consider neutral-axis elongation and multibody systems, if necessary, which can be used for various flutter harvester configurations in the future (e.g., extensible harvesters with fixed-fixed boundaries or multibody harvesters). For the electric formulation, we proposed an approach that is suitable for the superposition of finite element methods under the condition that the electric charge and voltage are constant only within each finite element of the piezoelectric patch. The second objective is to evaluate the validity of the framework through comparison with experiments conducted using a wind tunnel at the Institute of Fluid Science, Tohoku University, Japan. The remainder of this paper is organized as follows. Section 2 describes the formulation of the proposed flutter-harvesting analysis framework. The feasibility of the framework is verified in Section 3 by conducting wind tunnel experiments. Section 4 summarizes the conclusions of this paper.

Table 1
Considered methods in aeroelastic and piezoelectric studies based on ANCF.

	ANCF	UVLM	Piezoelectric effect	Experiment
Ref. [13,14]	Considered	-	Considered	Conducted
Ref. [15,16]	Considered	Considered	-	Conducted
Ref. [17]	Considered	Considered	-	-
Current study	Considered	Considered	Considered	Conducted

2. Piezoelectric flutter energy harvester model

The proposed method is besed on ANCF, a three-dimensional nonlinear UVLM [15], and a piezoelectric equation. This section provides a detailed explanation of ANCF, UVLM, and piezoelectric equations.

2.1. Absolute nodal coordinate formulation

Before modeling the flutter harvester based on ANCF, we conducted linear flutter stability analysis based on the plate element with torsional degrees of freedom and the doublet point method [18] and observed that the flutter harvester with the size considered in this study exhibited flutter owing to two-dimensional bending instability rather than torsional instability. Therefore, the harvester was modeled using two-dimensional ANCF beam elements without torsional degrees of freedom [9]. Three main advantages are associated with the use of ANCF. First, geometric nonlinearities were considered. Because flexible beams were used in this study, it was necessary to correctly simulate large finite element rotations. Second, the mass matrix was constant. The mass matrix may be computed only once in the dynamic analysis, which is computationally efficient for simulating LCO. Third, the UVLM aerodynamic panels and loading points may be easily derived from the structural elements of ANCF. In addition, the extensible beam theory and simple constraint equations of ANCF can contribute to designing more complicated flutter harvesters.

The ANCF beam element is shown in Fig. 2. The global coordinates of generalized vectors are defined as *XYZ* and the elastic deformation is represented by x in local coordinates. In the global coordinate system, the generalized vector $\boldsymbol{e}$ of ANCF is expressed as follows:

$$\boldsymbol{e} \equiv \left[\boldsymbol{r}|_{x=0}^{\mathrm{T}} \quad \boldsymbol{r}_x|_{x=0}^{\mathrm{T}} \quad \boldsymbol{r}|_{x=l}^{\mathrm{T}} \quad \boldsymbol{r}_x|_{x=l}^{\mathrm{T}} \right]^{\mathrm{T}}, \tag{1}$$

where $\boldsymbol{r}$ is the position vector, and l is the length of the finite element. An arbitrary position on an ANCF element can be expressed by a simple multiplication of the generalized nodal coordinate vector and shape function $\boldsymbol{S}(x)$ as follows:

$$\boldsymbol{r} \equiv \boldsymbol{S}(x)\boldsymbol{e}. \tag{2}$$

Using this equation, the UVLM aerodynamic panels and loading points can be easily derived. The Green–Lagrange strain $S_{\mathrm{GL}} \equiv (\| \boldsymbol{r}_x \|^2 - 1)/2$ was used for in-plane deformation. When considering the out-of-plane deformation, the Green–Lagrange strain of the in-plane deformation was assumed to be minimal. Therefore, $\| \boldsymbol{r}_x \| = 1$. The ANCF constant mass matrix $\boldsymbol{M}$ and linearized stiffness matrix $\boldsymbol{K} \equiv \partial \boldsymbol{F}_{\mathrm{elastic}}(\boldsymbol{e})/\partial \boldsymbol{e}$ were used to define Rayleigh damping $\boldsymbol{C} \equiv \alpha \boldsymbol{M} + \beta \boldsymbol{K}$

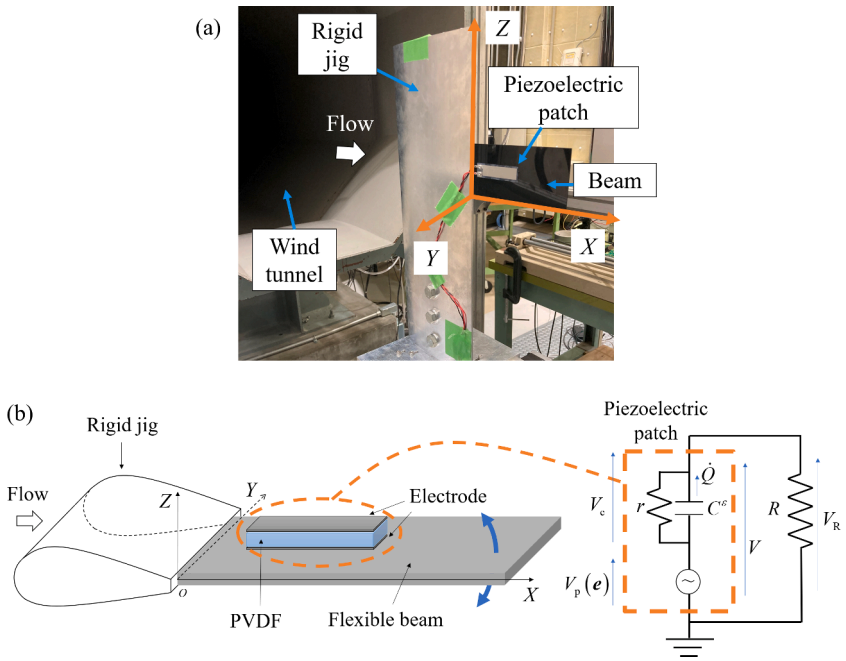

Fig. 1. (a) Flutter energy harvester using a piezoelectric patch. (b) Model of the flutter energy harvester.

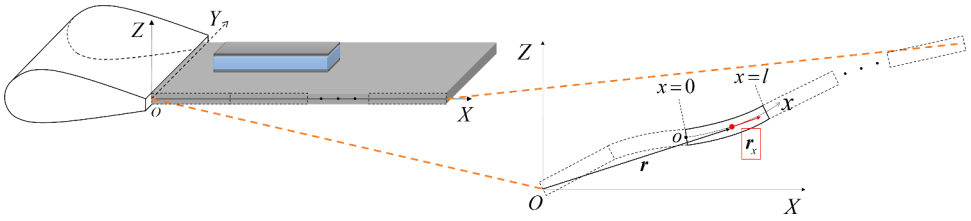

Fig. 2. Definition of the ANCF beam element.

[19], where $\boldsymbol{F}_{\text{elastic}}$ is the generalized elastic force vector, α is the mass-proportional coefficient, and β is the stiffness-proportional coefficient. Rayleigh damping and external forces owing to electricity and aerodynamics can be used to describe the equation of motion written as follows [9]:

$$\boldsymbol{M}\ddot{\boldsymbol{e}} + \boldsymbol{C}\dot{\boldsymbol{e}} + \boldsymbol{F}_{\text{elastic}}(\boldsymbol{e}) = \boldsymbol{F}_{\text{elec}}(Q) + \boldsymbol{F}_{\text{aero}}(\boldsymbol{e}, \dot{\boldsymbol{e}}), \tag{3}$$

where $\boldsymbol{F}_{\text{elec}}$ is the generalized electric force vector, and $\boldsymbol{F}_{\text{aero}}$ is the generalized aerodynamic force vector.

2.2. Unsteady vortex lattice method

Aerodynamic forces are represented using the UVLM, which is based on the potential flow theory by assuming inviscid and incompressible conditions. As shown in Fig. 3, the bound vortices around the flexible beam are represented by vortex panels in the UVLM. The bound vortex panel may be easily derived using Eq. (2). This is an advantage of combining ANCF and UVLM. The wake panel was released at each time step at the trailing edge, and it flowed at a local velocity. In the UVLM, the vortex strength was obtained using Eq. (4), which shows that the velocity normal to the bound vortex panel at the collocation point was zero [15].

$$\boldsymbol{A}\begin{bmatrix}\Gamma_{11}\\ \Gamma_{12}\\ \vdots\\ \Gamma_{mn}\\ \vdots\end{bmatrix} + \begin{bmatrix}(\boldsymbol{U}+\boldsymbol{w}_{11}-\boldsymbol{v}_{11})^{\mathrm{T}}\boldsymbol{n}_{11}\\ (\boldsymbol{U}+\boldsymbol{w}_{12}-\boldsymbol{v}_{12})^{\mathrm{T}}\boldsymbol{n}_{12}\\ \vdots\\ (\boldsymbol{U}+\boldsymbol{w}_{mn}-\boldsymbol{v}_{mn})^{\mathrm{T}}\boldsymbol{n}_{mn}\\ \vdots\end{bmatrix} = \boldsymbol{0}, \tag{4}$$

where $\boldsymbol{A}$ is the aerodynamic influence coefficient matrix obtained from Biot–Savart's law, $\boldsymbol{w}_{mn}$ is the induced velocity due to the wake panel, U is the uniform flow velocity, $\boldsymbol{v}_{mn}$ is the velocity of the harvester at the

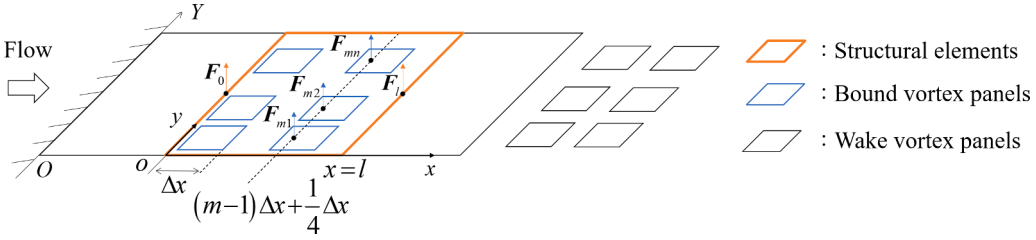

Fig. 3. Mapping of aerodynamic force.

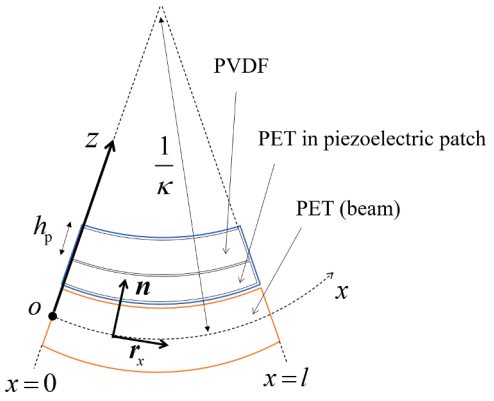

Fig. 4. Cross-section of the *x*-*z* plane.

collocation point obtained from generalized velocity, and *mn* is the number of aerodynamic panels in directions *x* and *y*, respectively. The aerodynamic force is obtained using Bernoulli's theorem based on the circulation of vortex panels Γ_{mn} obtained from Eq. (4). Thus, the aerodynamic force is a function of the flexible beam position and velocity, and generalized vectors and aerodynamic forces are nonlinear.

The aerodynamic force calculated using the UVLM was defined as acting on a quarter-chord length for each bound vortex panel, as shown in Fig. 3. This aerodynamic force must be converted into a generalized external force acting on the structural elements. Therefore, aerodynamic forces along the vortex panels were converted to those along the structural elements using the shape function as follows:

$$\boldsymbol{F}_{\text{aero}} \equiv [\,\boldsymbol{F}_0 \quad \boldsymbol{F}_l\,]^{\mathrm{T}} \equiv \sum_m \sum_n \boldsymbol{S}\{(m-1)\Delta x + \Delta x/4\}^{\mathrm{T}} \boldsymbol{F}_{mn}, \tag{5}$$

where $\boldsymbol{F}_{\text{aero}}$ is the generalized aerodynamic force vector acting on each structural node of a finite element, $\boldsymbol{F}_{mn}$ is the aerodynamic force acting on each bound vortex panel, and Δx is the length of the vortex panel, and $\boldsymbol{F}_0$ and $\boldsymbol{F}_l$ are, respectively, generalized aerodynamic force vectors at $x = 0$ and $x = l$.

2.3. Voltage equation

The *x*-*z* plane of the beam is shown in Fig. 4. The piezoelectric patch attached to the beam possesses electrodes in the *z*-direction. In this study, the electrodes were attached to the piezoelectric patch only in the *z*-direction, and the electric displacement caused by the bending deformation of the beam was the output. Considering the *x*-direction of the structure and the *z*-direction of electricity, the constitutive equation of piezoelectricity can be expressed as a scalar [20]:

$$\sigma_x \equiv c^D S_x - b_{\mathrm{p}} D_z \text{and} E_z \equiv -b_{\mathrm{p}} S_x + D_z / \varepsilon^S, \tag{6}$$

where σ_x is the stress in direction *x*, S_x is the bending strain in direction *x*, c^D is the constant-charge Young's modulus of the piezoelectric patch, E_z is the electric field in direction *z*, D_z is the electric displacement in direction *z*, ε^S is the constant–strain dielectric constant, and b_{p} is the piezoelectric constant. The piezoelectric potential energy of a finite element is expressed as follows:

$$\begin{aligned} U_{\mathrm{p}} &\equiv \textstyle\int_{V_0} (\sigma_x S_x + E_z D_z) \Big/ 2 dV_0 \\ &= \int_{V_0} \left(c^D \left(z \boldsymbol{n}^{\mathrm{T}} \boldsymbol{r}_{xx} \right)^2 - 2 b_{\mathrm{p}} z \boldsymbol{n}^{\mathrm{T}} \boldsymbol{r}_{xx} D_z + {D_z}^2 \Big/ \varepsilon^S \right) dV_0, \end{aligned} \tag{7}$$

where V_0 is the volume of an element in the piezoelectric patch, and the unit vector normal to the tangential direction of the beam $\boldsymbol{n} \equiv \begin{bmatrix} 0 & -1 \\ 1 & 0 \end{bmatrix} \boldsymbol{r}_x$ is expressed as shown in Fig. 4. The curvatures $\kappa = \boldsymbol{n}^{\mathrm{T}} \boldsymbol{r}_{xx} / \| \boldsymbol{n} \|^3$ and $\| \boldsymbol{n} \| = \| \boldsymbol{r}_x \| = 1$ were used in the study [12].

We removed the terms related to the variations in the electric displacement in Hamilton's principle and obtained the following equation:

$$\int_{t_1}^{t_2} \left(- \int_{V_0} \delta D_z \left(- b_{\mathrm{p}} z \boldsymbol{n}^{\mathrm{T}} \boldsymbol{r}_{xx} + D_z / \varepsilon^S \right) dV_0 + V_i \int_{A_i} \delta D_z dA_i \right) dt = 0, \tag{8}$$

where t_1 and t_2 are the specified times at which variation is zero, and *i* is the value related to the *i*th element in the piezoelectric patch. The electric field and displacement did not exhibit a constant distribution throughout the piezoelectric patch. In this study, the deformation within one finite element was assumed to be small, and the electric field and displacement were assumed to be constant only within the finite element, as shown in Fig. 5. These assumptions enabled independent calculations for each finite element. Therefore, the relationship between the electric charge and electric displacement can be approximated as $Q_i \equiv \int_{A_i} D_z dA_i \approx D_z A_i$, where A_i is the area horizontal to the *x*-*y* plane of the *i*th element of the piezoelectric patch, which yields the following equation:

$$\begin{aligned} -V_{\mathrm{p},i}(\mathbf{e}) + \left(C_i^S \right)^{-1} Q_i &= V_i, \\ \text{where } V_{\mathrm{p},i}(\mathbf{e}) &\equiv b_p \Big/ A_i \int_{V_0} z \boldsymbol{n}^{\mathrm{T}} \boldsymbol{r}_{xx} dV_0 \\ \text{and } C_i^S &\equiv \left(\int_z 1 \Big/ (A_i \varepsilon^S) dz \right)^{-1} = \varepsilon^S w_p l \Big/ h_p, \end{aligned} \tag{9}$$

Eq. (9) represents the voltage equation of the *i*th element, where $V_{\mathrm{p},i}(\boldsymbol{e})$ represents the voltage applied to the piezoelectric patch, w_{p} is the width of the piezoelectric patch, and h_{p} is the thickness of the piezoelectric patch.

The electric charge and voltage of the *i*th element were integrated into the electric charge and voltage of the piezoelectric patch. First, Eq. (9) is expressed as follows:

$$-\begin{bmatrix} V_{\mathrm{p},1}(\boldsymbol{e}) \\ V_{\mathrm{p},2}(\boldsymbol{e}) \\ \vdots \\ V_{\mathrm{p},N}(\boldsymbol{e}) \end{bmatrix} + \begin{bmatrix} C_i^S & & \boldsymbol{o} \\ & C_i^S & \\ \boldsymbol{o} & \ddots & \\ & & C_i^S \end{bmatrix}^{-1} \begin{bmatrix} Q_1 \\ Q_2 \\ \vdots \\ Q_N \end{bmatrix} = \begin{bmatrix} V_1 \\ V_2 \\ \vdots \\ V_N \end{bmatrix}, \tag{10}$$

where *N* denotes the number of structural divisions in the piezoelectric patch. We obtained the following equation by adding the rows and dividing by the number of elements:

$$\begin{aligned} &-\left(V_{\mathrm{p},1}(\boldsymbol{e}) + V_{\mathrm{p},2}(\boldsymbol{e}) + \cdots \right. \\ &\left. + V_{\mathrm{p},N}(\boldsymbol{e}) \right) / N + \left(C_i^S \right)^{-1} (Q_1 + Q_2 + \cdots + Q_N) / N = (V_1 + V_2 + \cdots + V_N) / N. \end{aligned} \tag{11}$$

The total electric charge is expressed as the sum of the elements, $Q \equiv Q_1 + Q_2 + \cdots + Q_N$. The total voltage is expressed as the average of the elements, $V \equiv (V_1 + V_2 + \cdots + V_N)/N$. The overall capacitance is expressed as the sum of the elements, $C^S \equiv N C_i^S$. The voltage applied to the structure is $V_{\mathrm{p}} \equiv \left(V_{\mathrm{p},1}(\boldsymbol{e}) + V_{\mathrm{p},2}(\boldsymbol{e}) + \cdots + V_{\mathrm{p},N}(\boldsymbol{e}) \right) / N$. The overall voltage equation is as follows:

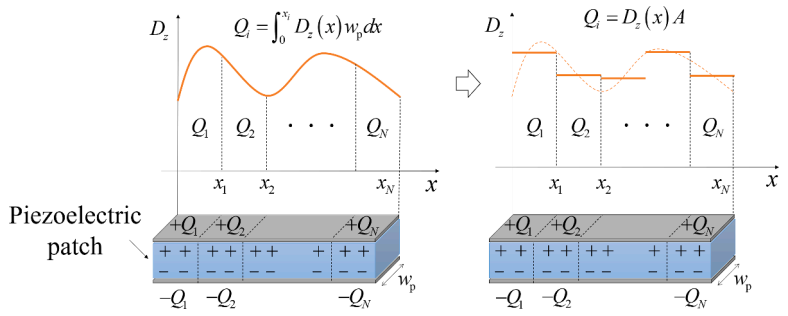

Fig. 5. Calculation of electric charge.

$$-V_{\mathrm{p}}(\boldsymbol{e}) + \left(C^{S}\right)^{-1} Q = V, \tag{12}$$

where C^S is the constant strain capacitance, Q is the electric charge, and V is the voltage.

In this study, we considered a circuit wherein only a resistor was connected to the piezoelectric patch, as shown in Fig. 1 (b). In addition, because we found that the electric charge leakage occurred inside the piezoelectric patch during the experiment, the parallel internal resistance was considered. Therefore, Eq. (12) is expressed only in terms of electric charge, as shown in Eq. (13). The resultant electric equation can be written as:

$$R\dot{Q} + (1 - R/r)\left(C^{S}\right)^{-1} Q = V_{\mathrm{p}}(\boldsymbol{e}), \tag{13}$$

where $V_{\mathrm{p}}(\boldsymbol{e})$ is the external voltage.

2.4. Proposed method

The flowchart in Fig. 6 illustrates the solution steps of the proposed method. First, the force $\boldsymbol{F}_{mn}$ of each aerodynamic panel was obtained using the UVLM. Next, each aerodynamic panel force, $\boldsymbol{F}_{mn}$, was transformed into a generalized coordinate force, $\boldsymbol{F}_{\mathrm{aero}}$, using Eq. (5). The equation of motion Eq. (3) and the voltage Eq. (13) were subsequently solved using the obtained aerodynamic force. This calculation was repeated until t became the ending time.

3. Experimental validation

Two experiments were conducted to evaluate the validity of the framework. The first was a free-vibration experiment on a beam with an attached piezoelectric patch. The second experiment included a flutter harvesting experiment wherein aerodynamic forces were considered. The experimental model consisted of polyethylene terephthalate (PET) as the beam and polyvinylidene difluoride (PVDF) as the piezoelectric patch. The deflection at the center of the beam was measured using a laser displacement sensor (LK-G400; Keyence, Japan). A measurement error of $\pm$ 1 $\times$ 10^{-4} m was included for displacement. The system was under a closed circuit, as shown in Fig. 1 (b). The voltage was measured using a voltage-measuring device (NR-HV04; Keyence). The sampling period was 2 $\times$ 10^{-5} s. The experimental setup is illustrated in Fig. 7, where the beam is clamped to a rigid wing-shaped jig. The adhesive gluing of the beam and piezoelectric patch was ignored in the analysis. The damping coefficient was estimated in two steps. In the first step, Rayleigh damping with a damping matrix defined as $\boldsymbol{C} = \alpha\boldsymbol{M} + \beta\boldsymbol{K}$ was employed, as described by Dong et al. [16]. The mass matrix M and the bending-related stiffness matrix K were constant in ANCF when the extensional deformation was small.

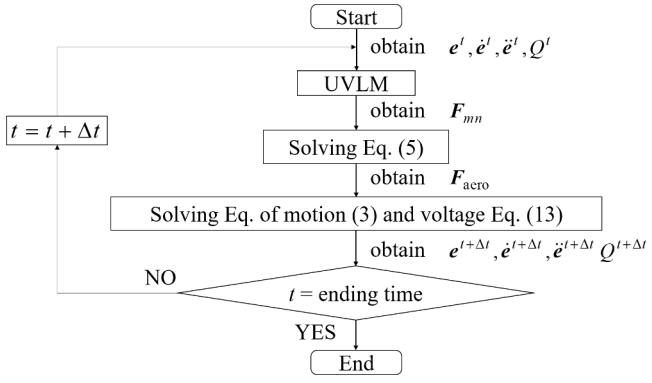

Fig. 6. Flowchart of the proposed method.

$$\begin{aligned} \alpha &\equiv 2\omega_1\omega_2(\zeta_1\omega_2 - \zeta_2\omega_1)/\left({\omega_2}^2 - {\omega_1}^2\right) \\ \beta &\equiv 2(\zeta_2\omega_2 - \zeta_1\omega_1)/\left({\omega_2}^2 - {\omega_1}^2\right) \end{aligned} \tag{14}$$

where ω_1 and ω_2 are the eigenangular frequencies of the first and second modes, respectively, and ζ_1 and ζ_2 are the damping ratios of the first and second modes, respectively. ζ_1 is calculated from the value of the free vibration peak. Because it was difficult to measure ζ_2, it was assumed to be equal to ζ_1, as stated by Dong et al. [16]. The second step was a trial-and-error tuning for α and β to reduce errors between the approximate and experimental values.

3.1. Free vibration

Free vibration experiments on beams with attached piezoelectric patches were performed and compared with the analysis to evaluate the validity of the simulation of structural and electric coupling. The experiments yielded a measurement error of $\pm$ 1 $\times$ 10^{-2} V for voltage. Table 2 lists the properties and values of the beam and piezoelectric patch.

Fig. 8 shows the time histories of free vibration experiments and analysis. The displacement of the center of the beam was measured in the Z-direction. During the free vibration experiment, an initial deflection of 0.04 m was applied at the center point, and the beam was started to vibrate at an initial value of 0 m/s. The voltage across the piezoelectric patch was measured and represented by V. The simulation results, including the phase difference between displacement and voltage, were in good agreement with the experimental results.

3.2. Flutter harvesting

Flutter harvesting was simulated and compared with experimental results using the proposed method. The wind tunnel experiment was conducted at the Institute of Fluid Science, Tohoku University, Japan. The voltage measurement device had a measurement error of $\pm$ 4 $\times$ 10^{-2} V. Table 3 lists the parameters used for flutter harvesting. The flow was in the axial direction. During the simulation, a constant distributed force, 9.3 $\times$ 10^{-2} N, was applied from 0 to 0.1 s to induce vibration. The root-mean-square (RMS) values were calculated for the displacement and voltage after LCO amplitudes converged. Fig. 9 (a) shows the

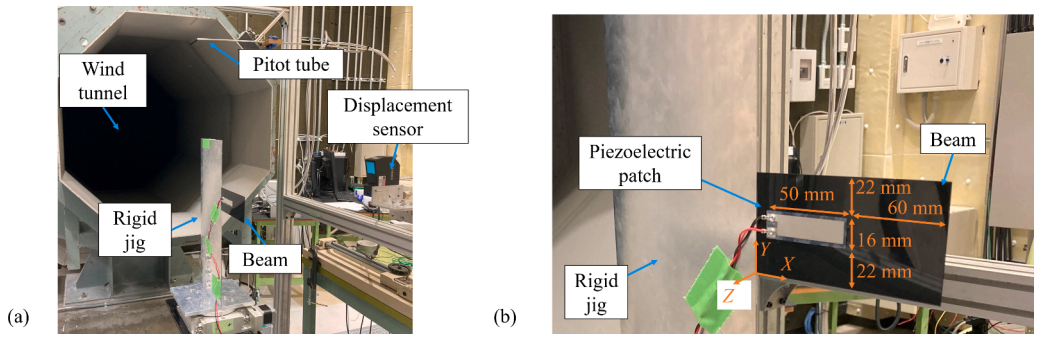

Fig. 7. (a) Overall view of the experimental apparatus and (b) an enlarged view of the harvester.

Table 2
Dimensions and material properties of beam and piezoelectric patch.

Property	Value	
	Beam	Piezoelectric patch
Material	PET	PVDF
Length	0.13 m	0.05 m
Width	0.06 m	0.016 m
Thickness	2.5×10^{-4} m	1.1×10^{-4} m (PVDF) 1.5×10^{-4} m (PET)
Density	1400 kg/m^3	1780 kg/m^3
Young's modulus	5.4 GPa	3.0 GPa
Number of elements	13	5
Damping parameter	$\alpha = 4.5$, $\beta = 1.3 \times 10^{-4}$	
Resistance	$R = 1$ MΩ	
Internal resistance	$r = 400$ MΩ	
Constant-strain dielectric constant	$\epsilon^S = 1.14 \times 10^{-10}$ F/m	
Piezoelectric constant	$b_p = 8 \times 10^{11}$ V/m	

relationship between flow velocity and displacement frequency. The numerical frequency was 23% lower than the experimental frequency. This may be attributed to the frictional force of the fluid. In this study, the effect of the viscosity was neglected because an inviscid UVLM was used. Tang and Païdoussis [21] investigated the impact of viscous drag in a flutter analysis. They stated that viscous drag stabilized the system, reduced the flutter amplitude, and increased the flutter frequency. The viscous drag directly affects the flutter frequency with respect to the beam tension. Hiroaki and Watanabe [22] simulated sheet flutter by considering nonlinear fluid frictional forces. In their study, they also stated that the fluid friction increased the frequency. The introduction of drag increases the tension in the longitudinal direction of the beam [21, 22], thereby increasing its stiffness and frequency in the bending direction due to the geometrical stiffening effect. The analysis accuracy is improved further by considering both the drag and drag-induced tension.

Fig. 9 (b) shows the relationship between the flow velocity and RMS displacement. The RMS displacements of the analysis were in good agreement with the experimental results. In the experiment, different hystereses of the flutter amplitude were observed when the flow velocity was increased and subsequently decreased. This phenomenon has also been observed in experiments conducted by other researchers [21]. A hysteresis is an experiment-specific phenomenon observed during buckling and undercooling. When a material transitions from an unstable equilibrium state to another state, it may not transition to the state where it should theoretically transition but to another state by applying a shock or slightly exceeding the theoretical state. Similarly, flutter may not occur experimentally, even at the flow velocities where flutter occurs theoretically.

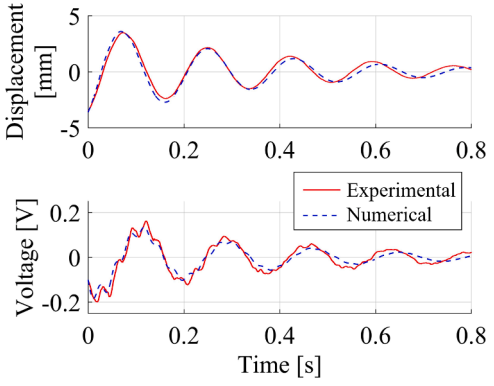

Fig. 8. Time histories of free vibration.

Fig. 9 (c) shows the relationship between the flow velocity and RMS voltage. The voltage was measured at both ends of the connected resistor. Hystereses were observed in the experimental results as well. The experimental and numerical results were in good agreement in terms of the shape of the graph.

4. Conclusions

In this study, a new flutter-harvesting analysis framework was developed based on ANCF, UVLM, and piezoelectricity. The framework considered the structural and aerodynamic nonlinearities caused by the large amplitude of the LCO and the three-dimensional aerodynamic effect. Only a few studies on flutter harvesting have attempted to satisfy the requirements of structural nonlinearity, aerodynamic nonlinearity, and three-dimensional aerodynamic forces. In addition, ANCF allows the consideration of neutral axis elongation and multibody motion, thus opening up the potential to simulate various flutter harvesters. The formulation in the developed framework is based on the assumption that the electric field and voltage within each finite element of the piezoelectric patch are constant. Therefore, it is suitable for the finite element method. The framework was validated using free-vibration and wind tunnel experiments. The frequency difference between the experiment and analysis was 23%. One of the reasons for this difference was that viscosity was not considered in UVLM. Therefore, the introduction of a viscous drag model will be analyzed in future studies. Furthermore, we investigated the quantitative advantages of the developed ANCF-based analysis framework through comparison with conventional analysis methods.

Table 3
Dimensions and material properties of beam and piezoelectric patch.

Property	Value
Fluid density	1.2 kg/m^3
Damping parameter	$\alpha = 4.5$, $\beta = 1.3 \times 10^{-4}$
Number of structural elements	13
Number of bound vortex panels	X direction: 52, Y direction: 14
Time step	1.0×10^{-4} s
Total wake length in X direction	0.13×1.5

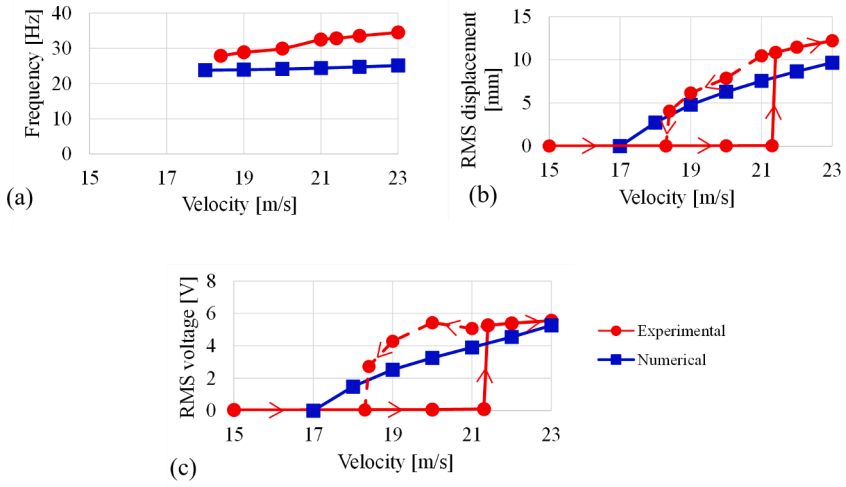

Fig. 9. Flow speed versus (a) frequency, (b) RMS displacement, and (c) RMS voltage.

CRediT authorship contribution statement

Taisei Mukogawa: Visualization, Validation, Methodology, Investigation, Formal analysis, Data curation, Conceptualization. **Kento Shimura:** Validation. **Shuonan Dong:** Validation. **Koji Fujita:** Writing – review & editing. **Hiroki Nagai:** Writing – review & editing. **Masaki Kameyama:** Writing – review & editing, Formal analysis. **Yu Shi:** Writing – review & editing. **Yu Jia:** Writing – review & editing. **Constantinos Soutis:** Writing – review & editing. **Hiroki Kurita:** Writing – review & editing. **Fumio Narita:** Writing – review & editing. **Yushin Hara:** Writing – review & editing. **Kanjuro Makihara:** Funding acquisition. **Keisuke Otsuka:** Supervision, Project administration, Funding acquisition.

Declaration of competing interest

The authors declare that they have no known competing financial interests or personal relationships that could have appeared to influence the work reported in this paper.

Acknowledgments

This work was supported by the Japan Society for the Promotion of Science (JSPS) KAKENHI (grant numbers 21K14341 and 22K18853), the Ebara Hatakeyama Memorial Foundation, the Nohmura Foundation for Membrane Structure Technology, the Mazak Foundation, and the JSPS Core-to-Core Program, A. Advanced Research Networks (JPJSCCA20200005). This study was supported by the Collaborative Research Project of the Institute of Fluid Science (IFS), Tohoku University (J23I013). We acknowledge the use of the IFS wind tunnel facility for our experiments.

Data availability

Data will be made available on request.

References

[1] H. Liang, G. Hao, O.Z. Olszewski, A review on vibration-based piezoelectric energy harvesting from the aspect of compliant mechanisms, Sens. Actuat. A: Phys. 331 (2021) 112743, https://doi.org/10.1016/j.sna.2021.112743.
[2] A. Abdelkefi, Aeroelastic energy harvesting: a review, Int. J. Eng. Sci. 100 (2016) 112–135, https://doi.org/10.1016/j.ijengsci.2015.10.006.
[3] J.M. McCarthy, S. Watkins, A. Deivasigamani, S.J. John, Fluttering energy harvesters in the wind: a review, J. Sound Vib. 361 (2016) 355–377, https://doi.org/10.1016/j.jsv.2015.09.043.
[4] J. Wang, L. Geng, L. Ding, H. Zhu, D. Yurchenko, The state-of-the-art review on energy harvesting from flow-induced vibrations, Appl. Energy 267 (2020) 114902, https://doi.org/10.1016/j.apenergy.2020.114902.
[5] J.A. Dunnmon, S.C. Stanton, B.P. Mann, E.H. Dowell, Power extraction from aeroelastic limit cycle oscillations, J. Fluids Struct. 27 (2011) 1182–1198, https://doi.org/10.1016/j.jfluidstructs.2011.02.003.
[6] S. Düssler, R. Palacios, Enhanced unsteady vortex lattice aerodynamics for nonlinear flexible aircraft dynamic simulation, AIAA J. 62 (2024) 1179–1194, https://doi.org/10.2514/1.J063174.
[7] D.M. Tang, D. Levin, E.H. Dowell, Experimental and theoretical correlations for energy harvesting from a large flapping flag response, J. Fluids Struct. 86 (2019) 290–315, https://doi.org/10.1016/j.jfluidstructs.2019.02.018.
[8] J. Gerstmayr, H. Sugiyama, A. Mikkola, Review on the absolute nodal coordinate formulation for large deformation analysis of multibody systems, J. Comput. Nonlinear Dyn. 8 (2013) 031016, https://doi.org/10.1115/1.4023487.
[9] A.A. Shabana, Dynamics of Multibody Systems, fifth ed., Cambridge University Press, Cambridge, 2020.
[10] K. Otsuka, K. Makihara, H. Sugiyama, Recent advances in the absolute nodal coordinate formulation: literature review from 2012 to 2020, J. Comput. Nonlinear Dyn. 17 (2022) 080803, https://doi.org/10.1115/1.4054113.
[11] R. Bulín, M. Hajžman, P. Polach, Nonlinear dynamics of a cable–pulley system using the absolute nodal coordinate formulation, Mech. Res. Commun. 82 (2017) 21–28, https://doi.org/10.1016/j.mechrescom.2017.01.001.
[12] J. Tao, A.E. Eldeeb, S. Li, High-fidelity modeling of dynamic origami folding using absolute nodal coordinate formulation (ANCF), Mech. Res. Commun. 129 (2023) 104089, https://doi.org/10.1016/j.mechrescom.2023.104089.
[13] A.A. Nada, A.M. El-Assal, Absolute nodal coordinate formulation of large-deformation piezoelectric laminated plates, Nonlinear Dyn. 67 (2012) 2441–2454, https://doi.org/10.1007/s11071-011-0158-4.
[14] X. Guo, J. Sun, L. Li, D. Zhang, Y. Chen, Large deformations of piezoelectric laminated beams based on the absolute nodal coordinate formulation, Compos. Struct. 275 (2021) 114426, https://doi.org/10.1016/j.compstruct.2021.114426.
[15] K. Otsuka, Y. Wang, K. Fujita, H. Nagai, K. Makihara, Multifidelity modeling of deployable wings: multibody dynamic simulation and wind tunnel experiment, AIAA J. 57 (2019) 4300–4311, https://doi.org/10.2514/1.J058676.
[16] S. Dong, K. Otsuka, K. Makihara, Hamiltonian formulation with reduced variables for flexible multibody systems under linear constraints: theory and experiment, J. Sound Vib. 547 (2023) 117535, https://doi.org/10.1016/j.jsv.2022.117535.
[17] A. Yamano, A. Shintani, T. Ito, C. Nakagawa, H. Ijima, Influence of boundary conditions on a flutter-mill, J. Sound Vib. 478 (2020) 115359, https://doi.org/10.1016/j.jsv.2020.115359.
[18] M. Kameyama, H. Fukunaga, Optimum design of composite plate wings for aeroelastic characteristics using lamination parameters, Comput. Struct. 85 (2007) 213–224, https://doi.org/10.1016/j.compstruc.2006.08.051.
[19] W.-S. Yoo, J.-H. Lee, S.-J. Park, J.-H. Sohn, O. Dmitrochenko, D. Pogorelov, Large oscillations of a thin cantilever beam: physical experiments and simulation using the absolute nodal coordinate formulation, Nonlinear Dyn. 34 (2003) 3–29, https://doi.org/10.1023/b:nody.0000014550.30874.cc.
[20] B. Jaffe, W.R. Cook Jr, H. Jaffe, Piezoelectric Ceramics, Academic Press, London, 1971.
[21] L. Tang, M.P. Païdoussis, On the instability and the post-critical behaviour of two-dimensional cantilevered flexible plates in axial flow, J. Sound Vib. 305 (2007) 97–115, https://doi.org/10.1016/j.jsv.2007.03.042.
[22] K. Hiroaki, M. Watanabe, Three-dimensional nonlinear analysis and wind-tunnel experiment of flutter generated on a rectangular sheet in uniform flow, J. Fluids Struct. 101 (2021) 103226, https://doi.org/10.1016/j.jfluidstructs.2021.103226.